Hyperfine Interactions 125 (2000) 45–68

Polarizer–analyzer optics

E.E. Alp, W. Sturhahn and T.S. Toellner

Advanced Photon Source, Argonne National Laboratory, Argonne, IL 60439, USA
E-mail: eea@aps.anl.gov

The principles behind the design and operation of polarization-based optics for nuclear resonant scattering of synchrotron radiation are discussed. With perfect single crystals and collimated X-rays emitted from undulator-based third-generation synchrotron radiation sources, polarization-selective optics with a sensitivity of parts per billion can be obtained. A general approach to optical activity is introduced, and the polarization dependence of the index of refraction is calculated for nuclear forward scattering for a medium with unidirectional symmetry. Some recent experimental results are reviewed and future applications are discussed.

Keywords: nuclear resonant scattering, synchrotron radiation, polarization, crystal optics

1. Introduction

Taking advantage of the transverse nature of electromagnetic waves and using a medium with strong optical activity, a sophisticated optical component was built to facilitate coherent nuclear resonant scattering experiments with synchrotron radiation. In this chapter, we will review the basic concepts related to the design of a particular kind of polarization-selective optics and some of the recent experiments exploiting this development.

The motivation for developing polarizer–analyzer-type optics for nuclear resonant forward scattering experiments came from the need to protect the detectors from the incident beam. The ratio of nuclear resonant and hence time-delayed photons to nonresonant, prompt photons in the case of an incident beam monochromatized to a bandpass of a few electron volts is typically of the order of 10^{-7}–10^{-10}. With the projected intensity of 10^{13}–10^{14} photons/s/eV produced from undulators of the third-generation sources, existing detectors would clearly not be able to handle such a flux. Therefore, a filter with an efficiency of 10^{7}–10^{9} was necessary. Polarization-selective optics can also be advantageously used to study magnetic phase transitions or to generate highly monochromatic X-ray beams with a bandpass of μeV. In this contribution, we will show that such optical components are possible for a number of Mössbauer isotopes in the 6–25 keV range.

Through the experiments of Young and Fresnel in the 19th century, and Maxwell's synthesis of empirical laws of electricity and magnetism, the propagation of electromagnetic fields as transverse waves has been firmly established. After the discovery

of X-rays in 1895 by Roentgen, experiments by Barkla [1,2], proved that, in the high-energy range of the electromagnetic spectrum corresponding to X-rays, the same rules applied. The fundamental coupling mechanism between an oscillating electric field and a charged particle allowed the description of scattered radiation as radiation emitted from an oscillating dipole[1] [3]. Hence, polarization-dependent characteristics like

(i) diffraction of X-rays from perfect crystals at the Brewster angle, and

(ii) rotation of polarization through an optically active medium

are relevant to our discussion.

The first characteristic mentioned above is related to the polarization-dependent diffraction of X-rays from single crystals, and it provides the necessary guidelines to design optical components to generate highly polarized X-rays with polarization purities in part-per-billion levels. The second aspect is related to the unique nature of nuclear resonance scattering, which strongly modifies the polarization state of X-rays absorbed and re-emitted by the nuclei. In the following, we will describe both of these features and explain how the successful implementation of the ideas strongly depended on the availability of high-brightness, undulator-based synchrotron radiation sources producing very collimated beams. The effects of X-ray source size and divergence in terms of storage ring and undulator parameters and the use of a collimating mirror to reduce the beam divergence will be reviewed. The section on optical activity and nuclear resonance is a general treatment of optical activity in the X-ray regime, and a particular application to nuclear resonant forward scattering for the case of unidirectional symmetry defined by magnetic field. Finally, we will discuss some of the published results.

2. Construction and optimization of an X-ray polarizer

The motivation and the method of designing a polarizer–analyzer type of optics for nuclear resonant scattering of synchrotron radiation have been described in detail previously [4–7]. The basic idea is to polarize the incident beam to a high degree in one state of polarization, then take advantage of the change in polarization state that occurs in a nuclear resonant medium, and finally suppress the nonresonant radiation in a crossed analyzer. The principles of how to achieve higher levels of polarization in the X-ray regime using perfect single crystals are given by Hart [8]. The detailed treatment of polarization of crystal waves under Bragg diffraction conditions are given by Batterman and Cole [9 and references therein]. The tunable polarizers for X-rays and neutrons were also discussed by Hart and Rodrigues [10]. We begin by explaining the relevant scattering geometry. Figure 1 shows the geometrical relation between the scattering vectors, $\mathbf{k}_{i,f}$, and the $\mathbf{p}_\sigma$ and $\mathbf{p}_\pi$ polarization vectors. The wave vector $|\mathbf{k}| = 2\pi/\lambda$; λ is the wavelength of the radiation, and $\mathbf{h}$ is a vector normal to the

[1] The original idea that the crystal is assumed to be built up of identical electric dipoles situated at the points of a perfect lattice belongs to P.P. Ewald.

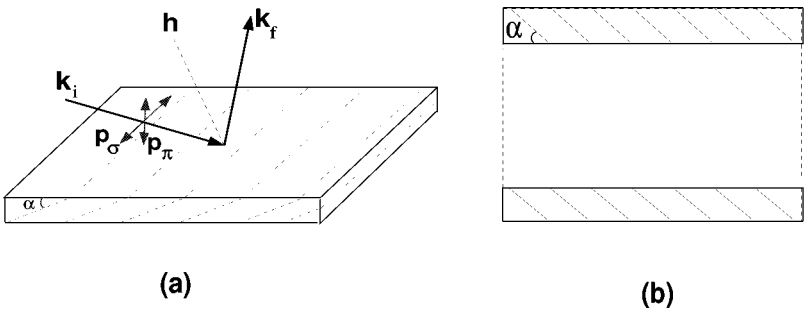

Figure 1. (a) Schematic of X-ray scattering geometry. Wave vectors of the incident and diffracted beams are $\mathbf{k}_i$ and $\mathbf{k}_f$. $\mathbf{p}_\sigma$ and $\mathbf{p}_\pi$ are the polarization components, θ_B is the Bragg angle, α is the asymmetry angle, and $\mathbf{h}$ is a vector normal to the diffraction plane. (b) The geometry for an asymmetrically cut channel-cut crystal with a Bragg angle near 45°.

diffraction planes. The reflected (i.e., diffracted) intensity from an infinitely thick single crystal around a Bragg angle is a function of the structure factor for incident and diffracted beams, Debye–Waller factor, asymmetry parameter, and polarization state of the incident beam. The reflectivity $R(\theta, E)$ of a single crystal near a Bragg diffraction point for a plane wave is a measure of scattering ability of the crystal over a certain angular and energy range. The explicit form of $R(\theta, E)$ for a monochromatic beam is given in the appendix. A more detailed treatment is given elsewhere in this book [11] based on the work of Zachariasen [12] and Warren [13]. Here, we will use the Si (8 4 0) reflection at 14.413 keV as an example because of the great interest in nuclear resonance of ^{57}Fe. The calculated reflectivities for $\mathbf{p}_\sigma$ and $\mathbf{p}_\pi$ polarizations are shown in figure 2.

The angular range over which the diffraction takes place is nonzero due to a finite number of lattice planes involved in scattering X-rays. The multiple scattering effects create a condition inside the crystal that prevents infinite penetration even if there were no absorption. This treatment, known as the dynamical diffraction theory, forms the basis of modern X-ray optics. It was orginally put forward by Darwin [14] and later developed by Ewald [15]. The reviews by James [3] and Batterman and Cole [9] are particularly illuminating. The effects predicted by the dynamical diffraction theory are only measurable in perfect or near-perfect crystals. In our case, silicon is a perfect crystal with a lattice spacing variation less than one part in 10^{-8}. The role of the asymmetry will be discussed later in this section. It will be sufficient to say that asymmetrically cut crystals are employed to increase the angular acceptance of the crystals to match incident beam angular divergence and to improve the polarization selectivity. The ratio of the area under the reflectivity curves for $\mathbf{p}_\sigma$ and $\mathbf{p}_\pi$ polarizations determines the polarization selectivity. The total intensity diffracted by a double-reflection channel-cut crystal is proportional to the product of single-crystal reflectivity $R_{\mathbf{p}_\sigma,\mathbf{p}_\pi}(\theta, E)$. Another factor that affects the overall performance is the spectral characteristics of the incident beam, typically expressed in terms of its angular distribution and its energy bandpass per unit time and per unit source size (expressed

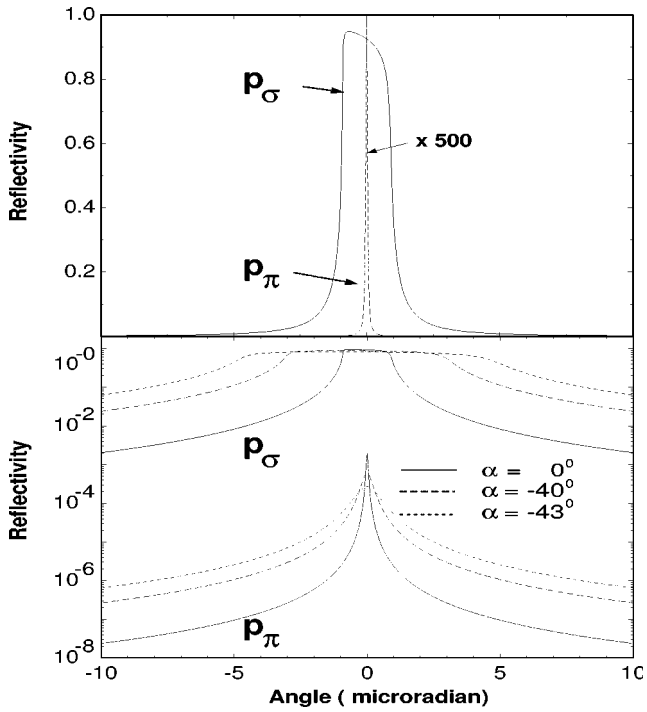

Figure 2. Reflectivity of Si (8 4 0) calculated at 14.413 keV as a function of angle for various asymmetry values and for $\mathbf{p}_\sigma$ and $\mathbf{p}_\pi$ polarizations. The $\mathbf{p}_\pi$ reflectivity in the upper panel is amplified to demonstrate the difference from the $\mathbf{p}_\sigma$ reflectivity. The logarithmic y-axis in the lower panel enables one to see both the relative weakness of $\mathbf{p}_\pi$ reflectivity as compared to $\mathbf{p}_\sigma$ polarized X-rays, as well as the angular range over which the diffraction condition is satisfied.

in units of photons/s/mm^2/mrad^2/eV). The common notation used suggests that this characteristic function is the spectral brilliance function $B(\theta, E)$. This should not be confused with the undulator brightness function, because the energy bandwidth is now limited by the first monochromator.

The flux transmitted by a channel-cut crystal can then be written as follows:

$$T_{(\mathbf{p}_\sigma,\mathbf{p}_\pi)} = \int\int R^2_{(\mathbf{p}_\sigma,\mathbf{p}_\pi)}(\theta, E_\circ + \varepsilon) B(\theta, E_\circ + \varepsilon)\, \mathrm{d}\theta\, \mathrm{d}\varepsilon. \tag{2.1}$$

The integration in eq. (2.1) over angle and energy around the Bragg angle, θ_B, and the Bragg energy, $E_\circ$, is best carried out numerically. The integration over energy around the resonance is limited either by the incident beam energy bandpass of the first monochromator or by the energy acceptance of the channel-cut crystal. This result follows from the formalism described by Toellner [11] when the asymmetry of the first and second faces of the polarizer and analyzer are the same but with opposite signs, leading to asymmetry parameters $b_2 = -1/b_1$, where 1 and 2 refer to the first and second faces. The asymmetry parameter b is defined in the appendix.

The reflectivity of $\mathbf{p}_\pi$-polarized monochromatic plane waves is much smaller than that of $\mathbf{p}_\sigma$-polarized waves for Bragg angles near 45°. Furthermore, when more than one reflection is used, this ratio is proportional to the power of number of reflections in the channel-cut crystal. For example, for channel-cut crystals with two reflections, the ratio of $\mathbf{p}_\pi$-to-$\mathbf{p}_\sigma$ reflectivities will be the square of the ratio obtained from a single reflection. Therefore, it is possible to push polarization purification of the incident beam as well as polarization analysis of the scattered beam to the desired level by increasing the number of reflections. In reality, the resonant scattering experiments require specific wavelengths at nuclear or electronic transitions. With the available choices of perfect crystals, it may not be possible to find reflections near the 45° Bragg angle. As the deviation from the ideal angle increases, the polarization selectivity will be significantly reduced. As a remedy, channel-cut crystals with weak links to offset the parallelity between the crystal planes were proposed, and it was shown that a high level of polarization selectivity could be reached, albeit with reduced throughput [10]. Siddons and others applied this approach to measure the Faraday rotation at Fe and Co K-absorption edges in magnetic materials [16].

Having described the polarization-dependent reflectivity of a channel-cut crystal, we can now write the degree of polarization purity for a beam diffracted by a channel-cut crystal as

$$\delta_0 = \frac{T_{\mathbf{p}_\pi}}{T_{\mathbf{p}_\sigma}}, \tag{2.2}$$

where transmitted flux T is defined for the channel-cut crystal in eq. (2.1). For the particular case of Si (8 4 0) at 14.413 keV, the calculated 3-dimensional angle–energy–reflectivity curves are shown in figure 3. The parameters used in reflectivity calculations are given explicitly in the appendix.

The polarization-based suppression of the nonresonant radiation is achieved by bringing a second polarizer channel-cut crystal to a crossed position to act as an analyzer, as shown in figure 4. Note that the incident beam produced by the undulator is linearly polarized in the storage ring plane, with a degree of polarization higher than 96%. This is not sufficient for suppression of nonresonant photons using just the analyzer after the nuclear resonant absorber, given the fact that the incident beam intensity exceeds 10^{13} Hz. However, by placing a polarizer channel-cut crystal before the sample, right after the pre-monochromator, the incident beam polarization purity δ_0 can approach one part in 10^{-8} as described in eq. (2.2).

The degree of suppression of σ-polarized radiation as a function of crossing angle Φ and δ_0 is given by

$$\delta(\Phi) = P_{\text{inc}} \cos^2 \Phi + \delta_0 \sin^2 \Phi, \tag{2.3}$$

where P_{inc} is the fraction of σ polarization in the incident beam and the second-order terms in δ_0 are ignored. Here, Φ represents the angle between the scattering planes of the polarizer and the analyzer. The adjustment of the crossing angle Φ becomes critical for $\delta_0 = 10^{-6}$ or smaller. For example, for $\delta_0 = 10^{-8}$ a deviation of 1 mrad

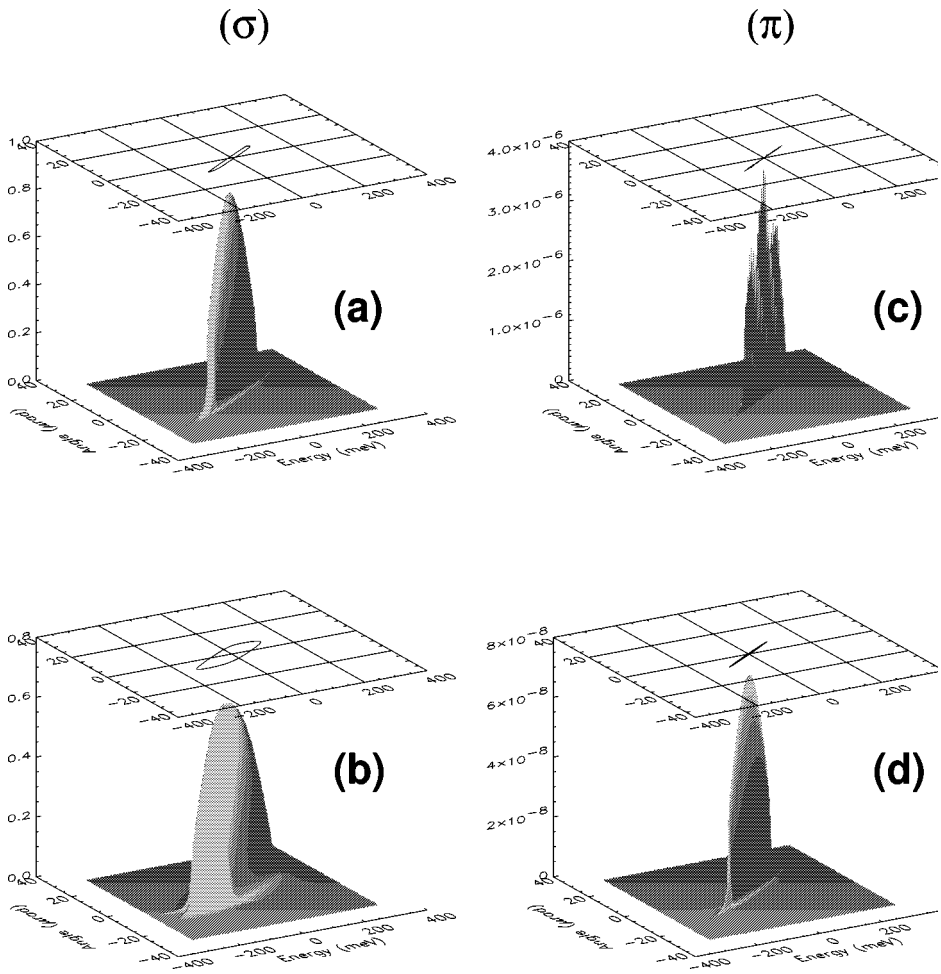

Figure 3. Angle–energy–reflectivity relationship for Si (8 4 0) channel-cut crystals for the (a) symmetric, (b) $\alpha = -43^\circ$ asymmetric case for $\mathbf{p}_\sigma$ polarization, and (c) symmetric, and (d) $\alpha = -43^\circ$ asymmetric case for $\mathbf{p}_\pi$ polarization. Notice the peak reflectivities of $\mathbf{p}_\sigma$ and $\mathbf{p}_\pi$ are six to eight orders of magnitude different, depending on asymmetry.

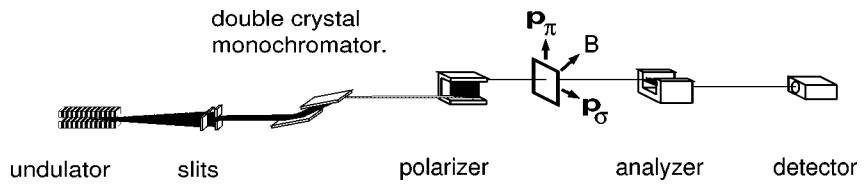

Figure 4. (a) The geometrical arrangement of polarizer–analyzer optics in forward scattering geometry. (b) The analyzer can be placed on a diffractometer arm and can be used after reflection from thin films, or diffraction from single crystals.

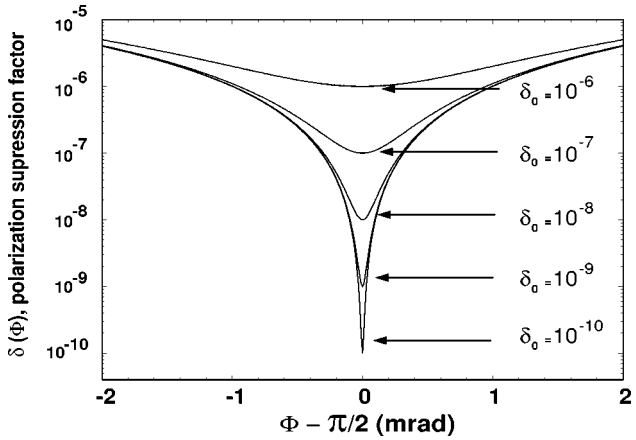

Figure 5. The degree of polarization-based suppression as a function of the crossing angle Φ, for various values of polarization purity δ_0 as defined in eqs. (2.2) and (2.3). δ_0 can be changed by varying the degree of asymmetry. $\delta(\Phi)$ will be ultimately limited by the horizontal divergence of the incident beam at the analyzer, the angular resolution of the goniometer, and the presence of other reflections in the same zone. These reflections have long Bragg tails, which will extend into the operational position of the analyzer.

from perfect alignment $\Phi = \pi/2$ may cause a change of two orders of magnitude in the polarization-based suppression of the prompt photons. This is demonstrated in figure 5.

We now return to the discussion of the role of asymmetry. At X-ray energies that are of interest for nuclear resonant scattering, the throughput of channel-cut crystals becomes an important issue due to limited angular acceptance. Also, a higher degree of polarization suppression may be needed as the incident beam flux increases by using longer undulators with optimized magnetic periods and with higher currents and optimized storage ring parameters. In order to improve the angular acceptance, as well as polarization selectivity, asymmetrically cut crystals were proposed [17]. The asymmetry parameter for a Bragg diffraction is defined in eq. (A.6) in the appendix, where α is the angle between the crystal planes and the surface of the crystal. The angular acceptance varies with asymmetry as follows:

$$(\Delta\theta)_{\text{asymmetric}} = \sqrt{b}(\Delta\theta)_{\text{symmetric}}. \tag{2.4}$$

Hence, as α approaches the Bragg angle, the Darwin width increases, while the peak reflectivity slightly decreases, mainly due to increased absorption. However, the integrated area under the reflectivity curves for σ- and π-polarized radiation changes strongly in favor of the σ component, as was shown in figures 2 and 3. Hence, the throughput of the polarizer increases due to increased angular acceptance increases, and its performance improves in terms of polarization purity and the ensuing suppression of the nonresonant radiation. The calculated results for different asymmetry values are tabulated in table 1. Here we define a somewhat arbitrary figure of merit to illustrate the effect of asymmetry on polarization selectivity. We compare the ratio of $T_{\mathbf{p}_\sigma}/T_{\mathbf{p}_\pi}$ for a

Table 1
The effect of asymmetry on $\mathbf{p}_\sigma$ and $\mathbf{p}_\pi$ reflectivity of Si (8 4 0) at 14.413 keV. Here, α is the asymmetry value in degrees, b is the asymmetry value as described in eq. (A.6), and $T_{\mathbf{p}_\sigma,\mathbf{p}_\pi}$ is the angle-energy integrated reflectivity for a channel-cut, double reflection crystal. The relative figure of merit is calculated as the ratio of $\mathbf{p}_\sigma$ and $\mathbf{p}_\pi$ reflectivity of a given asymmetric channel-cut crystal to that of a symmetric channel-cut crystal. The individual ratios of $T_{\mathbf{p}_\sigma}/T_{\mathbf{p}_\pi}$ can be taken as polarization selectivity for a channel-cut crystal.

α (deg)	b	T_σ (nrad-eV)	T_π (nrad-eV)	Relative figure of merit
0	1.0	273	$3.8 \cdot 10^{-5}$	1
-40	11.2	779	$2.1 \cdot 10^{-5}$	5
-43	27.3	1030	$1.0 \cdot 10^{-5}$	14
-44	52.1	1210	$5.5 \cdot 10^{-6}$	30

given asymmetry to that for the symmetric case, and we show that the performance can be improved by more than one order of magnitude by pushing the asymmetry value towards the Bragg angle. There is, however, a practical limit to the degree of asymmetry in channel-cut systems. When the values of b reach beyond a certain limit, the extra collimation may limit the throughput either by an inability to prepare the surface finish to the required levels or due to crystal strain. The approach presented here should be applicable in the energy range of 3–30 keV The tests performed to measure the effectiveness of the polarizer–analyzer have shown that, indeed, it is possible to reach the performance calculated from dynamical diffraction theory. The limited angular acceptance that prevented the use of polarizer–analyzer optics earlier is no longer prohibitive when a collimated source, such as synchrotron radiation produced by an undulator, is used. For example, the angular acceptance for Si (8 4 0) at 14.413 keV radiation is 1.9 μrad for the symmetric and 10 μrad for the asymmetric ($\alpha = -43°$) case. The latter is comparable to the angular divergence of the undulator radiation, which is around 10 μrad vertically and 40 μrad horizontally.

One major factor that may limit the polarization-based suppression is the presence of other reflections near the Bragg peak of interest. The long tails of the Bragg reflections, as shown in the logarithmic plot of reflectivity in figure 2, may cause transmission of part of the direct beam that was not converted from $\mathbf{p}_\sigma$ to $\mathbf{p}_\pi$ by nuclear resonance through the analyzer. These reflections, however small their reflectivity would be away from their exact Bragg condition, would still provide enough non-resonant $\mathbf{p}_\pi$ component leak-through to reduce the ultimate suppression achievable. Therefore, a procedure has been developed to avoid these reflections by cutting the crystals properly. The procedure to avoid unwanted reflections involves calculating the positions of all reflections with respect to a reference zone and cutting the crystal at an angle that might have a few degrees of clear zone, as described by Toellner [7]. Finally, the number of reflections can be increased from two to four to provide even larger polarization selectivity [10].

The type of X-ray optical component described here can be constructed at various energies using different reflections and different crystals. The choice of the material,

Table 2
Performance characteristics of channel-cut polarizers using $\Theta_B \approx 45^\circ$ Bragg reflections in silicon/germanium at selected Mössbauer transition energies.

Isotope	Energy (keV)	$\tau_{1/2}$ (ns)	Crystal reflection	Θ_B (deg.)	$\Delta\theta$[a] (μrad)	$\int R_\sigma^2\, d\theta$ (μrad)	δ_o
^{181}Ta	6.215	6800	Si(4 0 0)	47.28	142.0	59.8	5.5×10^{-4}
			Ge(4 0 0)	44.88	318.0	126.2	4.8×10^{-9}
^{169}Tm	8.410	4.0	Si(3 3 3)	44.85	44.4	19.0	1.2×10^{-8}
^{83}Kr	9.410	147	Si(5 3 1)	45.86	31.2	14.1	1.5×10^{-5}
^{57}Fe	14.413	97.8	Si(8 4 0)	45.10	10.2	6.1	1.0×10^{-8}
^{151}Eu	21.532	9.7	Ge(8 8 8)	44.87	0.78	0.15	1.7×10^{-9}
			Si(12 4 4)	44.69	0.31	0.26	9.1×10^{-6}
^{149}Sm	22.494	7.1	Ge(11 9 3)	45.07	0.55	0.05	6.0×10^{-11}
			Si(8 8 8)	44.68	0.25	0.21	9.7×10^{-6}
^{119}Sn	23.878	17.8	Ge(15 3 1)	44.73	0.35	0.03	1.6×10^{-8}
			Si(12 6 6)	44.63	0.19	0.16	1.5×10^{-5}

[a] The first four energies have the same crystal asymmetry factor; the angle between incident beam and crystal surface is 2°. The crystal reflections at the higher energies (>20 keV) are symmetrically cut.

whether Si, Ge, diamond, or saphhire, depends on the availability of high quality single crystals with negligible mosaicity or lattice space uniformity over several extinction depths perpendicular to the crystal planes and over the beam footprint on the crystal. A summary of such choices was described by Toellner and others [5]. In table 2 we present a simpler version for those Mössbauer isotopes in the range that is of current interest to us.

3. Source characteristics

Efficient operation of polarizer–analyzer optics requires that the incident beam divergence should be comparable to the angular acceptance of the crystals. The angular acceptance (the width of the reflectivity curves given in figure 2) can be manipulated to a certain extent by cutting the crystals asymmetrically, as we have seen in the previous section as well as elsewhere in this book [11]. Similarly, the characteristics of the incident beam can also be manipulated to a certain degree, even though this would require changes in the accelerator parameters and in the undulator periodicity.

The divergences of the X-rays for current synchrotron radiation sources are given by Mühlhaupt and Rüffer [18]. The angular divergence of the incident radiation has two contributions: the particle (i.e., electron or positron) beam divergence $\sigma'_{x,y}$ and the photon divergence for X-rays emitted from the undulator in the cone of the first or third harmonic, σ'_r. Here, the quantities related to divergence are indicated with a prime. The particle and radiative divergences can be added in quadrature to calculate

the overall divergence of the X-rays:

$$\Sigma'_{x,y} = \sqrt{\sigma'^2_{x,y} + \sigma'^2_r}. \tag{3.1}$$

The $\sigma'_{x,y}$, the Gaussian half-width of the divergence distribution, can be derived from the particle beam emittance $\varepsilon_{x,y}$ and beta-function $\beta_{x,y}$ by the following relationship:

$$\sigma'_{x,y} = \sqrt{\frac{\varepsilon_{x,y}}{\beta_{x,y}}}. \tag{3.2}$$

The emittance ε is the area of the phase space defined in terms of all position and angle values the particle beam may possess during its travel around the storage ring. It is expressed in units of distance·angle (meter·radian). Together with the beta-function $\beta_{x,y}$, which is the maximum amplitude of particle oscillations around the stable orbit at a given point d around the ring, and the emittance, $\varepsilon_{x,y}$, this is sufficient to define the source size:

$$\sigma_{(x,y)}(d) = \sqrt{\varepsilon_{x,y}\beta_{x,y}(d)}. \tag{3.3}$$

The terms beta particle, betatron oscillations, or β-function have historical origins, and they really refer to the stored particle motion in the ring. They are different for each storage ring. The β-functions of the storage rings with straight sections can also vary, and they can be individually adjusted; and hence they define the X-ray source characteristics emitted at that straight section where a particular insertion device is located. The vertical and horizontal emittance values are related to each other by a parameter called the coupling constant. Ideally, there is no coupling between these two quantities. However, due to misalignment of quadrupole magnets, there is a small but finite coupling [19]. The coupling constants of modern rings are about 1 percent or less, but this depends on the minimum gap of the undulators at a given time. It may be necessary to check the most recent values of emittance and source divergence at a given beamline to evaluate the performance of the optics. Values for the APS beamline 3-ID are given in table 3.

The undulator itself contributes to the radiation characteristics. The single electron radiation from an extended source along the direction of propagation has an opening angle given by the energy of the electrons in the ring, E (GeV), magnetic period λ_u, peak field $B_{\max}$ (kGauss) at a given undulator gap:

$$\sigma_{r'} = \sqrt{\frac{\lambda_n}{L}} = \frac{1}{\gamma}\sqrt{\frac{1 + (K^2/2)}{2Nn}}, \tag{3.4}$$

where N is the number of magnetic periods in the ring, n is the harmonic number of the radiation from the undulator (e.g., $1, 3, \ldots$), K is the deflection parameter of the undulator, L is the length of the undulator, λ_n is the wavelength of the nth harmonic, and γ is the electron energy divided by its rest mass energy.

The X-ray divergence can be dominated by the particle beam divergences or the radiative divergence, depending on the emittance of the ring. The relevant parameters

Table 3
Source and undulator characteristics at 3-ID beamline of the Advanced Photon Source.

Property	Unit	Value
Electron energy	GeV	7.0
Horizontal emittance (1σ)	nm · rad	6.5
Vertical emittance (1σ)	nm · rad	0.06
Horizontal source size (1σ)	μm	300
Vertical source size (1σ)	μm	30
Horizontal beta-function β_x	m	15.5 ± 3
Vertical beta-function β_y	m	6.3 ± 0.6
Measured horizontal divergence	μrad (FWHM)*	42
Measured vertical divergence	μrad (FWHM)	16.9
Calculated horizontal divergence	μrad (FWHM)	50
Calculated vertical divergence	μrad (FWHM)	12.7
Undulator period λ_u	cm	2.7
Length L	m	2.5
Number of magnetic periods N		90
Harmonic number n		1
Deflection parameter K at 14.4 keV		0.6
Relative energy $\gamma = E$ (GeV)/mc^2		13680

* FWHM for normal distribution corresponds to 1.66σ.

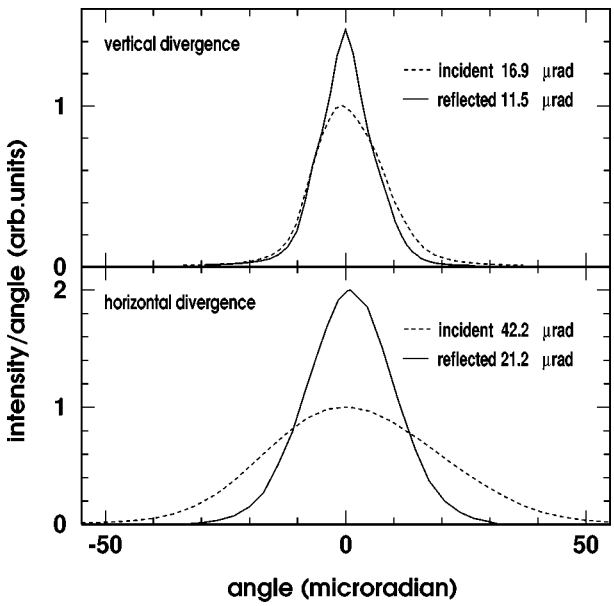

Figure 6. The measured vertical and horizontal beam divergence at the beamline 3-ID at the APS. The dashed line is the angular spread of the incident beam without the collimating mirror, and the solid line is beam divergence after the mirror. These measurements require an angular aperture of about 1 μrad and energy bandpass of about 10 meV, which can be provided by placing two high order reflection Si monochromators in an energy dispersive setting.

for the Advanced Photon Source ring are given in table 3. The numbers may vary slightly from the values given by Rüffer [18], which could be due to the dynamic nature of these rings.

Finally, there is also a chance to condition the X-ray beam for the polarizer–analyzer by further improving its collimation using a toroidal (bent cylindrical) mirror. This concept was tested at the APS 3-ID beamline of the Advanced Photon Source. The horizontal and vertical divergence of the incident beam, and the collimated beam are shown in figure 6. The divergence of the beam has been reduced by a combined factor of 2.8. The overall improvement in the throughput of the polarizer–analyzer was slightly less than a factor of 2. Nevertheless, clearly one can manipulate the beam divergence with grazing-incidence, total external-reflection mirrors.

4. Optical activity from nuclear resonances

The polarizer–analyzer optics that was introduced in the previous sections requires the insertion of an optically active material between polarizer and analyzer crystals. Such a material would have to convert part of the incident σ-polarized radiation such that a π-polarization component can be observed. We will now investigate under what conditions a material may show optical activity in the X-regime. For X-ray energies, materials may be characterized by an electric susceptibility tensor $\mathbf{\Psi}(\mathbf{x},\omega)$ depending on space coordinate and energy. The electric susceptibility defines a linear relation between the electric field and the polarizability of the material. The magnetic susceptibility is negligible. Then each energy component of the electric field inside the material satisfies

$$\begin{aligned} &\nabla\times\nabla\times\mathbf{E}(\mathbf{x},\omega)-\frac{\omega^2}{c^2}\mathbf{E}(\mathbf{x},\omega)=4\pi\frac{\omega^2}{c^2}\mathbf{\Psi}(\mathbf{x},\omega)\mathbf{E}(\mathbf{x},\omega),\\ &\nabla\cdot\left\{\big(1+4\pi\mathbf{\Psi}(\mathbf{x},\omega)\big)\mathbf{E}(\mathbf{x},\omega)\right\}=0. \end{aligned} \tag{4.1}$$

Given the smallness of the electric susceptibility for X-ray energies, the constraint posed by the second equation is well approximated by $\nabla\cdot\mathbf{E}=0$. This implies that an X-ray field propagating through a medium remains transverse. Now let us consider solutions of eq. (4.1) that are almost plane waves:

$$\mathbf{E}(\mathbf{x},\omega)=\mathbf{A}(\mathbf{x},\omega)\mathrm{e}^{\mathrm{i}\,\mathbf{k}\cdot\mathbf{x}}, \tag{4.2}$$

where $c|\mathbf{k}|=\omega$ and the function $\mathbf{A}$ shows a weak variation with position. Solutions of this type will properly describe the propagation of an X-ray field through matter if neither Bragg- nor Laue-excitations occur. We substitute the electric field into eq. (4.1) and use the approximate constraint to obtain

$$\begin{aligned} 2\mathrm{i}(\mathbf{k}\cdot\nabla)\mathbf{A}+\nabla^2\mathbf{A}&=-4\pi\frac{\omega^2}{c^2}\mathbf{\Psi}\mathbf{A},\\ \nabla\cdot\mathbf{A}+\mathrm{i}\mathbf{k}\cdot A&=0. \end{aligned} \tag{4.3}$$

The strongest spatial variation of the function **A** occurs in the direction of **k**, and one can neglect the second derivatives. With the notation $\mathbf{k} = \mathbf{s}\,\omega/c$, the field amplitude satisfies the first-order differential equation

$$\frac{\mathrm{d}}{\mathrm{d}\eta}\mathbf{A}(\mathbf{x}_0 + \eta\mathbf{s}, \omega) = 2\pi\mathrm{i}\,\frac{\omega}{c}\boldsymbol{\Psi}(\mathbf{x}_0 + \eta\mathbf{s}, \omega)\mathbf{A}(\mathbf{x}_0 + \eta\mathbf{s}, \omega), \tag{4.4}$$

where η takes the role of an affine parameter along the direction **s**. Assume a volume with almost constant field amplitude **A** exists almost everywhere in the medium. Then we can average eq. (4.4) over this volume, resulting in a formally identical equation that now contains an averaged susceptibility. If the medium is sufficiently homogeneous, the averaged susceptibility will be independent of location, and the averaged version of eq. (4.4) can be integrated. The solution is

$$\mathbf{A}(\mathbf{x}_0 + \eta\mathbf{s}, \omega) = \exp\left\{2\pi\mathrm{i}\eta\frac{\omega}{c}\overline{\boldsymbol{\Psi}}(\omega)\right\}\mathbf{A}(\mathbf{x}_0, \omega), \tag{4.5}$$

where $\overline{\boldsymbol{\Psi}}(\omega)$ denotes the spatially averaged susceptibility tensor. The previous equation combined with eq. (4.2) results in the compact expression

$$\mathbf{E}(\mathbf{x}, \omega) = \exp\big\{\mathrm{i}\mathbf{k}\cdot(\mathbf{x} - \mathbf{x}_0)\mathsf{N}(\omega)\big\}\mathbf{E}(\mathbf{x}_0, \omega) = \mathsf{T}(\mathbf{x} - \mathbf{x}_0, \omega)\mathbf{E}(\mathbf{x}_0, \omega), \tag{4.6}$$

where the index of refraction $\mathsf{T} = 1 + 2\pi\overline{\boldsymbol{\Psi}}$ was introduced. If the electric field is known at position $\mathbf{x}_0$, one may calculate the field everywhere inside the material using the transmission function T. However, according to eq. (4.2) the field must be almost a plane wave, a property that is retained. The electric field is also transverse throughout the medium, i.e., $\mathbf{k}\cdot\mathbf{E} = 0$. The index of refraction, as well as the transmission function, are second-rank tensors in normal space. In eq. (4.6), the transversality of the electric field permits one to treat them like second-rank tensors in the 2-dimensional subspace defined by the plane normal to **k**. The projection of the index of refraction into this subspace, n, has a unique decomposition in terms of the Pauli spin-matrices

$$\mathsf{n} = (1 - \mathbf{s}\otimes\mathbf{s})\mathsf{N}(1 - \mathbf{s}\otimes\mathbf{s}) = \frac{1}{2}\mathrm{Trace}(\mathsf{n}) + \sum_{j=1}^{3} a_j\sigma_j, \tag{4.7}$$

where the coefficients a_j depend on the traceless part of n only. With this expansion and the use of the properties of the Pauli spin-matrices, the transmission function may be converted to a form suitable for further discussion:

$$\mathsf{T} = \mathrm{e}^{\mathrm{i}\phi n_0}\left\{\cos\phi\xi + \mathrm{i}\frac{\sin\phi\xi}{\xi}(\mathsf{n} - n_0)\right\} \tag{4.8}$$

with

$$n_0 = \frac{1}{2}\,\mathrm{Trace}(\mathsf{n}), \qquad \phi = \mathbf{k}\cdot(\mathbf{x} - \mathbf{x}_0), \qquad \xi = \sqrt{n_0^2 - \det(\mathsf{n})}. \tag{4.9}$$

The transmission function given in the form of eq. (4.8) permits us to calculate the optical activity of the medium in terms of the index of refraction. Let $\{\mathbf{p}_\sigma, \mathbf{p}_\pi, \mathbf{s}\}$ be an

orthonormal basis in normal space. The X-rays are propagating along **s**, and the other basis vectors give the two possible directions of linear polarization. Optical activity is then, e.g., described by the matrix element $T_{\pi\sigma} = \mathbf{p}_\pi \mathsf{T} \mathbf{p}_\sigma$, which transforms incident σ-polarized radiation into π-polarized radiation. Equation (4.8) shows that this matrix element will be proportional to the quadratic form $\mathbf{p}_\pi \mathsf{n} \mathbf{p}_\sigma = \mathbf{p}_\pi \mathsf{N} \mathbf{p}_\sigma$. In many cases, the medium possesses global symmetries, e.g., a uniformly magnetized material showing axial symmetry or an isotropic medium with cubic symmetry. These situations can be conveniently addressed after the index of refraction tensor is expressed as the sum of irreducible tensor operators of rank zero (the trace), rank one (the antisymmetric part), and rank two (the symmetric traceless part). The relevant matrix elements are then

$$\mathbf{p}_\pi \mathsf{N} \mathbf{p}_\sigma = \mathbf{p}_\pi \mathsf{N}_A \mathbf{p}_\sigma + \mathbf{p}_\pi \mathsf{N}_S \mathbf{p}_\sigma = \mathbf{p}_\sigma \mathsf{N} \mathbf{p}_\pi + 2 \mathbf{p}_\pi \mathsf{N}_A \mathbf{p}_\sigma . \tag{4.10}$$

For systems with cubic symmetry, these matrix elements vanish, and optical activity is not possible. In the case of uniaxial symmetry, one obtains after some manipulations

$$\begin{aligned} \mathbf{p}_\pi \mathsf{N}(\omega) \mathbf{p}_\sigma &= n_1(\omega) \cos\theta + n_2(\omega) \sin^2\theta \sin 2\varphi , \\ \mathbf{p}_\sigma \mathsf{N}(\omega) \mathbf{p}_\pi &= -n_1(\omega) \cos\theta + n_2(\omega) \sin^2\theta \sin 2\varphi , \end{aligned} \tag{4.11}$$

where θ is the polar angle and φ is the azimuthal angle of the symmetry direction in the basis $\{\mathbf{p}_\sigma, \mathbf{p}_\pi, \mathbf{s}\}$. The functions n_1 and n_2 are energy-dependent material properties. Equation (4.11) properly describes the optical activity of a uniformly magnetized sample, where the symmetry direction is the direction of the magnetic field. Only for the special directions $\theta = (l+1/2)\pi$, $\varphi = l\pi/2$ with integer l, does the optical activity vanish by symmetry. Another interesting case presents itself if three orthogonal mirror planes exist. One calculates for the relevant matrix elements

$$\begin{aligned} \mathbf{p}_\pi \mathsf{N}(\omega) \mathbf{p}_\sigma &= \mathbf{p}_\sigma \mathsf{N}(\omega) \mathbf{p}_\pi \\ &= n_{20}(\omega) \sin^2\beta \sin 2\gamma + 2 n_{22}(\omega) \sin^2\beta \cos 2\gamma \sin 2\alpha , \end{aligned} \tag{4.12}$$

where $\{\alpha, \beta, \gamma\}$ are the Euler angles needed to rotate the triad of mirror plane normals into the basis $\{\mathbf{p}_\sigma, \mathbf{p}_\pi, \mathbf{s}\}$. Again the functions n_{20} and n_{22} are energy-dependent material properties. The optical activity of a resonant nucleus exposed to the electric field gradient of its environment, for example, is described by eq. (4.12). A single-domain antiferromagnet shows both axial symmetry and mirror plane symmetry, and the optical activity of such a material is therefore given by eq. (4.12) with $n_{22} = 0$. The angles β, γ describe the orientation of the symmetry axis.

So far our discussion has been quite general, e.g., no reference was made to the nature of the electric susceptibility and how to calculate the functions n_1 and n_2 in eq. (4.11). In this paper, we are concerned with nuclear resonant forward scattering. The nuclear contribution to the index of refraction can be derived from the forward scattering amplitude. From the formulas of Sturhahn and Gerdau [20] one obtains

$$\mathsf{n}(\omega) = \frac{1}{2} \rho \sigma_N F \sum_{mm'} \frac{\mathsf{W}_{mm'}(\mathbf{s})}{z_{mm'}(\omega) - \mathrm{i}} , \tag{4.13}$$

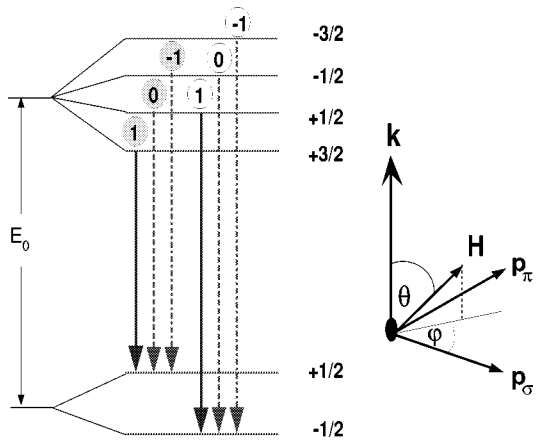

Figure 7. Magnetic nuclear level splitting for the 14.413 keV transition of ^{57}Fe. This situation presents a special case of unidirectional symmetry.

where ρ is the area density of resonant nuclei in the direction of **s**, σ_N is the nuclear resonant cross section, and F is the Lamb–Mössbauer factor. The sum is over all sublevels of nuclear ground and excited states. The function $z_{mm'} = 2\hbar(\omega_{mm'} - \omega)/\Gamma$ depends on the energy difference between excited and ground states $\hbar\omega_{mm'}$ and the nuclear level width Γ. The weight of each resonance at $\hbar\omega_{mm'}$ is given by the second-rank tensor $\mathsf{W}_{mm'}$. The weights are normalized by $\sum_{mm'} \mathsf{W}_{mm'} = 1$. We now focus on the study of the 14.413 keV transition of ^{57}Fe. In figure 7, a schematic of the nuclear ground and excited states is shown for a case of unidirectional symmetry induced by a magnetic field. For this case of pure magnetic hyperfine interactions, the weights take the simple form

$$\mathsf{W}_{m,m+M}(\mathbf{s}) = \frac{8\pi}{3} C^2\big(II'1; mm+M\big)\mathbf{Y}^{(0)}_{1M}(\mathbf{s}) \otimes \mathbf{Y}^{(0)*}_{1M}(\mathbf{s}), \tag{4.14}$$

where I, I' are spin quantum numbers of nuclear ground and excited states, $\mathbf{Y}^{(0)}_{1M}$ gives the vector spherical harmonic representing the M1 multipole transition of ^{57}Fe, and $C(\ldots)$ are Clebsch–Gordan coefficients in the notation of Rose [21]. The representation of the weight tensors in the previously chosen basis $\{\mathbf{p}_\sigma, \mathbf{p}_\pi, \mathbf{s}\}$ is now easily calculated from the vector spherical harmonics:

$$\begin{aligned}
\mathbf{Y}^{(0)}_{11}(\mathbf{s}) &= \sqrt{\frac{3}{16\pi}}\big\{\mathbf{p}_\sigma(-\cos\varphi + \mathrm{i}\sin\varphi\cos\theta) - \mathbf{p}_\pi(\sin\varphi + \mathrm{i}\cos\varphi\cos\theta)\big\},\\
\mathbf{Y}^{(0)}_{10}(\mathbf{s}) &= \mathrm{i}\sqrt{\frac{3}{8\pi}}\sin\theta\{\mathbf{p}_\sigma\sin\varphi - \mathbf{p}_\pi\cos\varphi\},\\
\mathbf{Y}^{(0)}_{1,-1}(\mathbf{s}) &= \sqrt{\frac{3}{16\pi}}\big\{\mathbf{p}_\sigma(-\cos\varphi\cos\theta + \mathrm{i}\sin\varphi) - \mathbf{p}_\pi(\sin\varphi\cos\theta + \mathrm{i}\cos\varphi)\big\},
\end{aligned} \tag{4.15}$$

where the angles θ and φ determine the direction of the magnetic field. The optical activity of the nuclear resonant medium is caused by the off-diagonal terms given by

$$\mathbf{p}_\pi \mathsf{W}_{m,m\pm1}\,\mathbf{p}_\sigma = \frac{1}{2}C^2\big(I\,I'\,1; m\,m\pm1\big)\big\{\pm\sin\varphi\cos\varphi\sin^2\theta + \mathrm{i}\cos\theta\big\},$$
$$\mathbf{p}_\pi \mathsf{W}_{mm}\mathbf{p}_\sigma = -C^2(I\,I'\,1; m\,m)\sin\varphi\cos\varphi\sin^2\theta. \tag{4.16}$$

The first equation comprises the effect of the $M = \pm1$ transitions on the optical activity, whereas the second line gives the contribution of the $M = 0$ terms. When eq. (4.16) is inserted into eq. (4.13), an expression of the form given by eq. (4.11) emerges, as we expected from earlier symmetry arguments. The material-dependent functions are obtained from the nuclear properties and exhibit resonant behavior:

$$n_1(\omega) = \frac{\mathrm{i}}{4}\rho\sigma_N F\sum_m\left\{\frac{C^2(I\,I'\,1; m\,m+1)}{z_{m,m+1}(\omega)-\mathrm{i}} + \frac{C^2(I\,I'\,1; m\,m-1)}{z_{m,m-1}(\omega)-\mathrm{i}}\right\},$$
$$n_2(\omega) = \frac{1}{8}\rho\sigma_N F\sum_m\left\{\frac{C^2(I\,I'\,1; m\,m+1)}{z_{m,m+1}(\omega)-\mathrm{i}} - \frac{2C^2(I\,I'\,1; m\,m)}{z_{mm}(\omega)-\mathrm{i}}\right.$$
$$\left. - \frac{C^2(I\,I'\,1; m\,m-1)}{z_{m,m-1}(\omega)-\mathrm{i}}\right\}. \tag{4.17}$$

In addition, we give the functions n_0 and ξ from eq. (4.9) that are needed to calculate the transmission function $T_{\pi\sigma}$:

$$\xi(\omega) = \sqrt{n_2^2(\omega)\sin^4\theta - n_1^2(\omega)\cos^2\theta},$$
$$n_0(\omega) = \frac{1}{8}\rho\sigma_N F\sum_m\left\{\big(1+\cos^2\theta\big)\frac{C^2(I\,I'\,1; m\,m+1)}{z_{m,m+1}(\omega)-\mathrm{i}}\right.$$
$$\left. + 2\sin^2\theta\frac{C^2(I\,I'\,1; m\,m)}{z_{mm}(\omega)-\mathrm{i}} + \big(1+\cos^2\theta\big)\frac{C^2(I\,I'\,1; m\,m-1)}{z_{m,m-1}(\omega)-\mathrm{i}}\right\}. \tag{4.18}$$

After calculating the index of refraction for a particular case of unidirectional symmetry, we return now to a more general discussion of the transmitted intensity, which is the usual result of an experiment. First, we need a satisfactory model for the radiation field that is incident on the sample, and we adopt the model of Sturhahn and Kohn [22] for monochromatized synchrotron radiation (SR). The X-rays emitted by the present SR sources can be understood as an incoherent superposition of one-photon fields. This does not change by employment of crystal optics, and the individual one-photon fields henceforth will be called "SR components". It is then safe to apply the transmission function to each SR component and perform an incoherent average over their individual properties, i.e., when calculating intensities. For each SR component, the coherence length for all directions in space is much larger than the size of the nucleus. This is caused by a large distance between nucleus and SR source, as well as by the monochromatization process. In addition, we will assume that the transverse coherence length of the SR components is larger than the typical dimension of the averaging

volume that led us to eq. (4.5). The incident field may then be represented by a plane quasimonochromatic wave with wave vector $\mathbf{k}$, average energy $\overline{\omega} = c|\mathbf{k}|$, and a time-dependent amplitude, i.e., $\mathbf{E}(\mathbf{x}_0, t) = \mathbf{p}_\sigma a(t) \exp(\mathrm{i}\mathbf{k}\cdot\mathbf{x}_0 - \mathrm{i}\,\overline{\omega}t)$. The unit vector $\mathbf{p}_\sigma$ gives the time-independent polarization of the SR component. The function $a(t)$ describes the pulse structure of the SR component, as well as its energy spectrum including the modification by crystal optics. We assume that $a(t) = 0$ outside the time interval $[t_0, t_0+\delta t]$, i.e., the SR component arrives at time t_0 at the sample and has a duration δt. The duration shall be much smaller than the nuclear lifetime and the inverse of the typical nuclear level splitting. The set $\{\mathbf{k}, \mathbf{p}_\sigma, a(t)\}$ presents a unique description of the SR component. The contribution of the SR component to the intensity per time unit, after it passed through the resonant material and the analyzer crystal, is given by

$$\frac{\mathrm{d}I(t)}{\mathrm{d}t} = \left| \int R_{\pi\sigma}\big(t - t'\big) a\big(t'\big)\,\mathrm{d}t' \right|^2 . \tag{4.19}$$

The response function R is related to the transmission function of eq. (4.8) as follows:

$$R_{\pi\sigma}(t) = \mathrm{e}^{-\mathrm{i}\,\overline{\omega}t} \int T_{\pi\sigma}(\omega)\mathrm{e}^{-\mathrm{i}\,\omega t}\frac{\mathrm{d}\omega}{2\pi}. \tag{4.20}$$

The nuclear resonant part of the transmission function is restricted to a narrow energy region such that its Fourier image given by eq. (4.20) is constant during the SR pulse. Under the reasonable assumption that the electronic contribution to the optical activity vanishes at the nuclear transition energy, eq. (4.19) can be simplified to

$$\frac{\mathrm{d}I}{\mathrm{d}t} = B_0 \big| R_{\pi\sigma}(t - t_0) \big|^2 = B_0 \left| \int \mathbf{p}_\pi \mathrm{n} \mathbf{p}_\sigma \mathrm{e}^{-\mathrm{i}\,\omega(t-t_0)} \mathrm{e}^{\mathrm{i}\phi n_0} \frac{\sin\phi\xi}{\xi} \frac{\mathrm{d}\omega}{2\pi} \right|^2 . \tag{4.21}$$

Here $B_0 = |\int a(t)\,\mathrm{d}t|^2$ is the spectral intensity of the incident SR component. The functions n_0 and ξ depend on energy and were defined in eq. (4.9). For resonant material of thickness L in the direction of the incident radiation, we obtain $\phi = L\overline{\omega}/c$. In general, the integral in eq. (4.21) has to be evaluated numerically. Analytic solutions were given for special cases, e.g., by Shvyd'ko et al. [23] for well separated nuclear sublevels.

5. Experimental results and discussion

Successful demonstration of the polarizer–analyzer optics for nuclear resonant scattering studies had to await the availability of the undulator sources. This was mainly due to the narrow energy width of the resonance, which is less than 1 μeV, as compared to electronic resonance of the order of 1 eV. Therefore, one of the early experiments with a polarizer–analyzer optics [16] using a bending magnet radiation source was the measurement of Faraday rotation in Co at 7.709 keV with a set of Si (4 2 2) channel-cut crystals used as polarizer and analyzer. This technique was later used to measure magnetic moments on Fe in Fe_3Pt invar alloys [17], among others. The

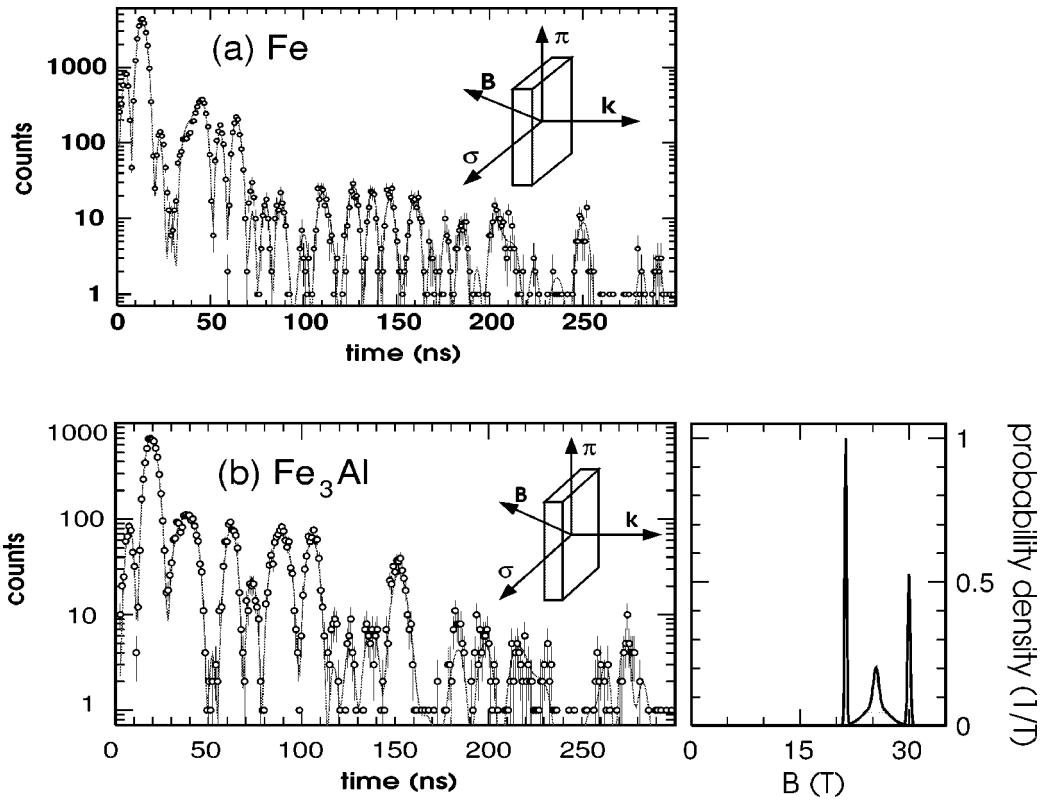

Figure 8. The time spectra of (a) α-Fe, and (b) Fe_3Al, obtained using polarizer/analyzer optics described in figure 4. The solid lines are fits obtained by including the proper polarization geometry using the CONUSS program, as described in [20]. This allows one to extract the internal hyperfine field strengths and field distributions, as shown in the right-hand figure.

first application in nuclear resonant scattering was carried out at an undulator source [5] on a storage ring that was not optimized for low emittance. The primary purpose of the early measurements was to evaluate the efficiency of the polarization filtering, determine the prompt/delayed ratio, and see how close to the origin of excitation the nuclear resonant signal can be observed.

The experiments conducted at the NE3 beamline of the KEK-Accumulator ring in 1994 are shown in figure 8. In these measurements the sample was placed at 90° to the photon propagation direction, and the external magnetic field was oriented to be 45° to the σ and π directions [5]. The thickness of the Fe foil (95% ^{57}Fe) was 10.6 μm, yielding an effective bandpass of $36\,\Gamma_\circ$. The ratio of nonresonant, prompt, to resonant, delayed photons was 0.62. The Fe_3Al foil was 10 μm, and it was similarly enriched. The avalanche photodiode detector used in these measurements had a time resolution of 0.7 ns. The total count rate was 18 Hz in a time window of 2–500 ns. Similar measurements were also carried out at ESRF by Siddons et al. [6], where they

observed 1200 Hz counts with a background of 200 Hz upon tuning the photon energy through the nuclear resonance.

In order to evaluate the performance of the polarizer–analyzer, we can combine the reflectivity calculations, presented earlier in table 1, and the source characteristics presented in table 3. It should be recognized that the roles of σ and π are interchanged for the polarizer and analyzer, respectively. The transmission is calculated using a program developed by one of us (TT). Recently, it was shown that the SHADOW program can also be used for this type of calculations [24]. The tests performed at the APS so far have produced a maximum of 5 kHz measured after the analyzer when a 10.6 μm thick ^{57}Fe foil is placed between the polarizer and analyzer. This represents about 20–30% of what is predicted from the computations. The sources of the discrepancy are external factors at the beamlines, like crystal preparation quality, the time structure of the ring, and the detector efficiencies.

The ability to observe close to origin has been exploited in a relaxation study of $(NH_4)Al(SO_4)_2{\cdot}12H_2O$ by Leupold et al. [25]. This system is a model compound for investigation of the temperature dependence of the electron spin–lattice relaxation phenomenon [26]. Five percent of Al is substituted by ^{57}Fe to use the resonant nuclei as a probe. The nuclear forward scattering experiments with and without polarizer are shown in figure 9.

Another experiment that takes advantage of the polarizer/analyzer optics is described in great detail in this book [28]. The idea of a tunable spectrometer with μeV resolution has proven to be elusive in the hard X-ray range, and the effort exploiting the optics described here is one of the avenues recently pursued. By using a rapidly rotating disk coated with ^{57}Fe, the energy of the reflected beam can be tuned by Doppler shifting. The geometry is grazing incidence total reflection with a magnetic field oriented in the direction of photon propogation. It is, then, possible to generate an X-ray beam with approximately $50\,\Gamma$ (0.25 μeV) bandwidth, including the effects of σ-to-π conversion, and the increase in the nuclear decay rate due to large effective thickness. When the external magnetic field is parallel to the photon propagation direction the optical activity is maximized (see eqs. (4.12), (4.18) and (4.19)), and the π-component can be filtered from the rest of the photons via the polarizer–analyzer optics. The performance of the system and the details are described in [27,28].

The polarizer–analyzer optics was used in a recent experiment [29] to measure the temperature range of the spin reorientation phase transition in Fe_3BO_6. The ferriborate is a weak ferromagnet with an orthorhombic crystal structure in which all Fe is in the $+3$ state. There are two magnetically distinct sites with an occupation ratio of 2 : 1. The Curie temperature is 508 K, and the spin reorientation transition T_s is around 142°C (415 K). Below this temperature the spins of the (a)-site, $\mathbf{s}^a$, are oriented along the c-direction [0 0 1] with a slight canting in the plane perpendicular to the b-direction [0 1 0], giving a net magnetization $\mathbf{M}$ along the a-direction [1 0 0], as shown in figure 10(a). Above T_s the spins of the (a)-site, $\mathbf{s}^a$, are oriented

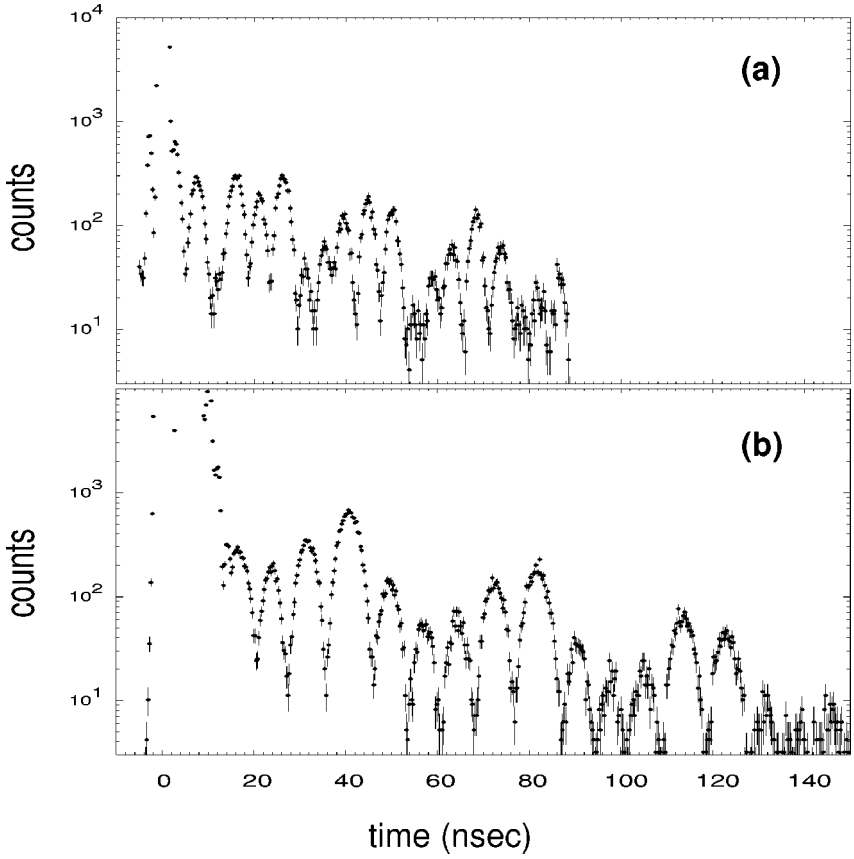

Figure 9. The time spectra of $(NH_4)Al_{0.95}{}^{57}Fe_{0.05}(SO_4)_2 \cdot 12H_2O$ at 4 K in a 2 T magnetic field, (a) σ-to-π scattering using polarizer–analyzer optics, and (b) without polarizer–analyzer. $H_{\rm ext} \parallel \vec{k}$ in both cases. Data taken from [25].

along the a-direction, [1 0 0], with a slight canting in the plane perpendicular to the b-direction, [0 1 0], giving a net magnetization **M** along the c-direction, [0 0 1]. When the crystal is oriented such that the photons are parallel to [1 0 0] and the polarization plane is along [0 1 1], i.e., 45° in the bc-plane, then below $T_{\rm s}$, σ to π conversion occurs. Above $T_{\rm s}$, σ-to-π transition is not allowed, and the transmitted intensity through the crossed analyzer will be reduced to background. The result is shown in figure 10(b). The special oven built for this purpose provided the required temperature stability and resolution to carry out the experiment. While the result obtained from this experiment was consistent with the previous experiments using a polarized, single line ^{57}Co source [30], the deviation at 141.1 K was not explained. However, the fact that the transition takes place over 1 degree rather than abruptly answers some of the questions posed earlier with respect to broadening of the spin reorientation transition temperature range in impurity-doped Fe_3BO_6 [31].

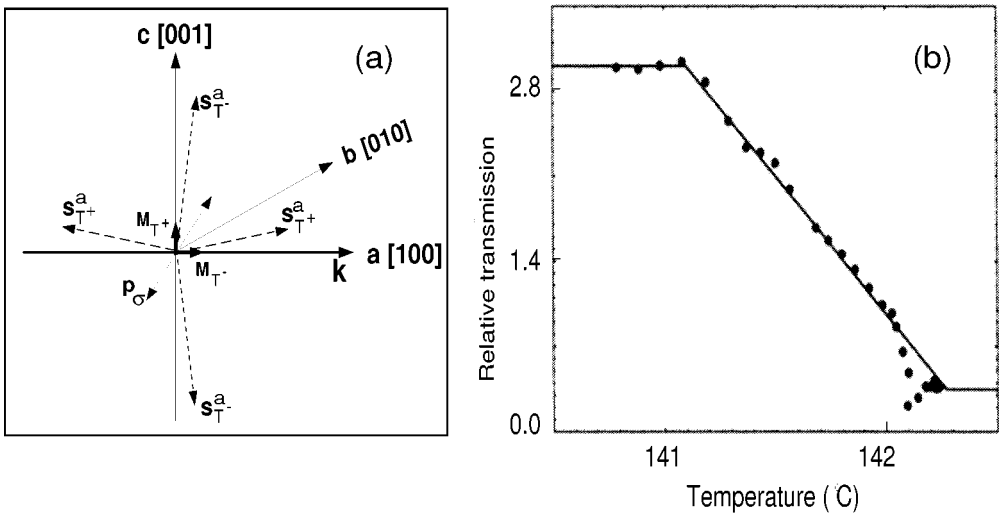

Figure 10. (a) Directions of spin moments **s** and net magnetization **M** above and below the spin transition temperature T_s in Fe_3BO_6. (b) The relative transmission of photons through the analyzer as a function of temperature around the spin phase transition [29].

6. Conclusions

The polarizer–analyzer described here represents a unique example of crystal optics suitable for a high-brightness sources. The longstanding angular mismatch between the divergence of the incident beam and the limited angular acceptance of crystals is remedied by the use of undulator radiation and by improving the angular acceptance by asymmetric cutting. The strong optical switching via excitation of a nuclear resonance while maintaining the beam brilliance either through a Bragg diffraction, forward scattering or specular reflection provides a suitable geometry for a similar crystal to be used as an anlayzer. Thus, the degree of polarization-based selectivity exceeds previous attempts by orders of magnitude and opens the possibility for new kinds of experiments.

Acknowledgements

The authors would like to thank Prof. S. Kikuta and Prof. M. Ando for providing access to the beamline at KEK-AR NE3, Dr. X. Zhao and Y. Yoda for their help during the measurements, and Dr. O. Leupold for providing the data shown in figure 9. We also thank Prof. E. Gerdau for the permission to use unpublished data presented in figure 10. The work at Argonne is supported by US DOE BES Materials Science, Contract number W-31-109-ENG-38.

Appendix

The reflectivity of a single crystal around a Bragg diffraction is given in reduced angular coordinate L as follows:

$$R(L) = L - \sqrt{(L^2 - 1)}, \tag{A.1}$$

where

$$L = \frac{1}{1+\kappa^2}\left[W^2 + g^2 + \left[\left(W^2 - g^2 - 1 + \kappa^2\right)^2 + 4\left(gW - \kappa\right)^2\right]^{1/2}\right]. \tag{A.2}$$

Furthermore, W and g can be defined in terms of the complex susceptibility Ψ, polarization factor P, kinematic Bragg angle Θ_{B}, and asymmetry parameter b as follows:

$$W = \frac{1}{2}\left(\sqrt{b} + \frac{1}{\sqrt{b}}\right)\frac{\Psi_{or}}{P|\Psi_{Hr}|} + \sqrt{b}\frac{\sin 2\Theta_{\mathrm{B}}}{P|\Psi_{Hr}|}(\Theta - \Theta_{\mathrm{B}}), \tag{A.3}$$

where

$$g = \frac{1}{2}\left(\sqrt{b} + \frac{1}{\sqrt{b}}\right)\frac{\Psi_{oi}}{P|\Psi_{Hr}|}, \tag{A.4}$$

$$\kappa = \frac{|\Psi_{hi}|}{|\Psi_{hr}|}, \tag{A.5}$$

$$b = \frac{\sin(\Theta_{\mathrm{B}} + \alpha)}{\sin(\Theta_{\mathrm{B}} - \alpha)}. \tag{A.6}$$

Here, the asymmetry angle α is defined as the angle between crystal surface and the Bragg planes. $P = 1$ for σ-polarization and $P = \cos(2\Theta_{\mathrm{B}})$ for π-polarization.

$$\Psi_{Hr} = -\frac{r_e\lambda^2}{\pi V}\sum_j \left(f_H + f'\right)\mathrm{e}^{2\pi\mathrm{i}\vec{H}\vec{R}_j} f_{\mathrm{DW}}^j\left(\vec{H}\right), \tag{A.7}$$

$$\Psi_{Hi} = -\frac{r_e\lambda^2}{\pi V}\sum_j (f'')\mathrm{e}^{2\pi\mathrm{i}\vec{H}\vec{R}_j} f_{\mathrm{DW}}^j\left(\vec{H}\right), \tag{A.8}$$

Table 4
The parameters used in the calculation of crystal reflectivity.

a_{Si}	5.431 Å
Θ_{B}	45.104°
λ	0.86023 Å
$f_{H=0}$	14
$f_{H=(840)}$	3.6
f'	0.113862
f''	0.105055
f_{DW}	0.73
m_{Si}	$4.6495 \cdot 10^{-23}$ g
Θ_{D}	543 K

where $\Psi_{(r,i)}$ refer to real and imaginary parts of the complex susceptibility, $\vec{H}$ represents the reciprocal lattice vector, f' and f'' are the real and imaginary parts of the dispersion corrections due to photoabsorption, and they are given in [32]. The f_{DW}^{j} is the Debye–Waller factor to account for lattice vibrations forcing the atoms to stay away from their equilibrium positions, and hence, reducing the scattering strength. An expression for silicon is given in [32,33], which is given in table 4, along with other parameters used in the calculation of eq. (2.1).

References

[1] C.G. Barkla, Phil. Trans. A 204 (1905) 467.
[2] C.G. Barkla, Proc. R. Soc. 77 (1906) 247.
[3] R.W. James, Solid State Phys. 63 (1963) 57.
[4] E.E. Alp, SPIE Proc. 1740 (1993) 1967.
[5] T.S. Toellner, E.E. Alp, W. Sturhahn, T.M. Mooney, X. Zhang, M. Ando, Y. Yoda and S. Kikuta, Appl. Phys. Lett. 67 (1995) 1993.
[6] D.P. Siddons, J.B. Hastings, U. Bergmann, F. Sette and M. Krisch, Nucl. Instrum. Methods B 103 (1995) 371.
[7] T.S. Toellner, Ph.D. thesis, Northwestern University, IL (1996).
[8] M. Hart, Phil. Mag. B 38 (1978) 41.
[9] B.W. Batterman and H. Cole, Rev. Mod. Phys. 36 (1964) 681.
[10] M. Hart and A.R.D. Rodrigues, Phil. Mag. B 40 (1979) 149.
[11] T.S. Toellner, this issue, section VI-1.
[12] W.H. Zachariasen, *Theory of X-Ray Diffraction in Crystals* (Wiley, New York, 1945).
[13] B.E. Warren, *X-Ray Diffraction* (Addison-Wesley, Reading, MA, 1969) (Reprinted by Dover, New York, 1990).
[14] C.G. Darwin, Phil. Mag. 27 (1914) 315; and (1914) 675.
[15] P.P. Ewald, Ann. Phys. 49 (1916) 117; 54 (1917) 159.
[16] D.P. Siddons, M. Hart, Y. Amemiya and J.B. Hastings, Phys. Rev. Lett. 64 (1990) 1967.
[17] E.E. Alp, M. Ramanathan, S. Salem-Sugui, Jr. and F. Oliver, Rev. Sci. Instrum. 63 (1992) 1221.
[18] G. Mühlhaupt and R. Rüffer, this issue, section II-1.
[19] M. Cornacchia, in: *Synchrotron Radiation Sources: A Primer*, ed. H. Winick (World Scientific, Singapore, 1994).
[20] W. Sturhahn and E. Gerdau, Phys. Rev. B 49 (1994) 9285.
[21] M.E. Rose, *Elementary Theory of Angular Momentum* (Wiley, New York, 1967).
[22] W. Sturhahn and W. Kohn, this issue, section III-2.2.
[23] Y. Shvyd'ko, U. van Bürck, W. Potzel, P. Schindelmann, E. Gerdau, O. Leupold, J. Metge, H.D. Rüter and G.V. Smirnov, Phys. Rev. B 57 (1998) 3552.
[24] M.S. del Rio, SPIE Proc. 3448 (1998) 230.
[25] O. Leupold, A. Bernhard, E. Gerdau, J. Jäschke, H.D. Rüter, H. de Waard, E.E. Alp, P. Hession, M. Hu, W. Sturhahn, J. Sutter, T. Toellner, H. Grünsteudel, W. Meyer, S. Schwendy, A.X. Trautwein, H. Winkler, A.I. Chumakov, J. Metge and R. Rüffer, Hyp. Interact. 113 (1998) 81.
[26] S.C. Bhargava, J.E. Knudsen and S. Mœrup, J. Phys. C 12 (1979) 2879.
[27] R. Röhlsberger, E. Gerdau, R. Rüffer, W. Sturhahn, T.S. Toellner, A.I. Chumakov and E.E. Alp, Nucl. Instrum. Methods A 394 (1997) 251.
[28] R. Röhlsberger, this issue, section VII-2.
[29] A. Bernhard, Diplomarbeit, University of Hamburg (1996).
[30] R. Wolfe, R.D. Pierce, M. Eibschutz and J.W. Nielsen, Solid State Commun. 7 (1969) 949.

[31] M. Hirano, T. Okuda, T. Tsushima, S. Umemura, K. Kohn and S. Nakamura, Solid State Commun. 15 (1974) 1129.
[32] *International Tables for Crystallography, Vol. C: Mathematical, Physical, and Chemical Tables*, ed. A.C. Wilson (Kluwer Academic, Dordrecht, 1992).
[33] B.C. Larson, J.Z. Tischler and D.M. Mills, J. Mater. Res. 1 (1986) 144.